

Supplemental Material for: Floquet phonon lasing in multimode optomechanical systems

Laura Mercadé,¹ Karl Pelka,² Roel Burgwal,^{3,4} André Xuereb,² Alejandro Martínez,¹ and Ewold Verhagen^{4,3}

¹Nanophotonics Technology Center, Universitat Politècnica de Valencia, Camino de Vera s/n, 46022 Valencia, Spain

²Department of Physics, University of Malta, Msida MSD 2080, Malta

³Department of Applied Physics and Institute of Photonic Integration,

Eindhoven University of Technology, P.O. Box 513, 5600 MB Eindhoven, The Netherlands

⁴Center for Nanophotonics, AMOLF, Science Park 104, 1098 XG Amsterdam, The Netherlands

(Dated: July 1, 2021)

I. ANALYTICAL TREATMENT OF THE MEAN FIELD

The separation of the quantum Langevin equations result in the dynamics for the mean fields

$$\begin{aligned}\dot{\alpha} &= \left\{ -i \left[\Delta - \sum_{j=1}^N g_j R(\beta_j) \right] - \frac{\kappa}{2} \right\} \alpha + \mathcal{E}_0 \mathcal{T} e^{-i\phi_0}, \\ \dot{\beta}_j &= - \left(i\Omega_j + \frac{\Gamma_j}{2} \right) \beta_j + ig_j |\alpha|^2,\end{aligned}\quad (1)$$

complementary to the fluctuations in Eq. (2) of the main text. The periodically modulated drive $\mathcal{T}(t) = \sum_k \mathcal{T}_k e^{-ik\Omega_{\text{mod}} t}$ ($k \in \mathbb{Z}$) turns the differential equations into a periodic ones and admits a Floquet ansatz such that we express α as a truncated Fourier series $\alpha(t) = \sum_n \alpha_n e^{-in\Omega_{\text{mod}} t}$ with $n \in \{-D, \dots, D\}$ and find that Eq. (1) reduces to the dynamical system

$$\dot{\alpha}_m = \mathcal{E}_0 \mathcal{T}_m - \tilde{\chi}_{\text{cav},m}^{-1} \alpha_m + \sum_{(p,q)} \chi_{\text{cub},q}^{-1} \alpha_p \alpha_p^* \alpha_{p-q} \alpha_{m-q}, \quad (2)$$

where $p \in \{-D, \dots, D\}$, $q \in \{-D + p, \dots, D + p\}$, and the solutions of the mechanical mean fields $\beta_j(t)$ follow from their solutions in Fourier space

$$\beta_j(t) = \frac{ig_j}{2\pi} \int d\omega \frac{|\tilde{\alpha}|^2(\omega)}{i(\omega - \Omega_j) - (\Gamma_j/2)} e^{-i\omega t}, \quad (3)$$

with $|\tilde{\alpha}|^2(\omega) = \sum_{(p,q)} \alpha_p \alpha_{p-q}^* \delta(\omega - iq\Omega_{\text{mod}})$. Here, we defined $\tilde{\chi}_{\text{cav},m}^{-1} = i(\Delta - m\Omega_{\text{mod}}) + \frac{\kappa}{2}$, and $\chi_{\text{cub},q}^{-1} = \sum_j \chi_{\text{OM},j}^{-1}(q\Omega_{\text{mod}})$, with $\chi_{\text{OM},j}^{-1}(\omega)/g_j^2 = [i(\omega - \Omega_j) - \frac{\Gamma_j}{2}]^{-1} - [i(\omega + \Omega_j) - \frac{\Gamma_j}{2}]^{-1}$. The steady state $\tilde{\alpha}_m$, which is the basis of the Floquet treatment of the fluctuations in Eq. (3) of the main text has to be found by solving $\dot{\alpha}_m = 0$. This task constitutes the solution of $2D + 2$ coupled real cubic equations which can be done analytically for $D = 0$ employing methods from algebraic geometry and has to be done numerically beyond $D = 0$.

II. TRANSFER CHARACTERISTIC OF INTENSITY MODULATION

The optical intensity modulation underlying the theoretical description is based on the imbalanced single-drive Mach-Zehnder modulator depicted in Fig. 1(a). Our discussion follows the descriptions of [1, 2]. It consists of a Mach-Zehnder

interferometer realized with two waveguides and an electro-optic phase modulator implemented in one waveguide. The output field of such a Mach-Zehnder modulator is given by

$$\mathcal{E}_{\text{out}}(t) = \frac{\mathcal{E}_{\text{in}}(t) e^{i\phi_0}}{2} (1 + e^{i\phi_{\text{mod}}(t)}) \quad (4)$$

where \mathcal{E}_{in} is the input field and ϕ_0 an input phase offset. The electro-optic phase modulator causes the phase-shift $\phi_{\text{mod}}(t) = \pi V(t)/V_\pi$ when a voltage $V(t)$ is applied, where V_π is a characteristic of the modulator. The intensity transfer characteristic for $\mathcal{E}_{\text{in}}(t) = \mathcal{E}_0 e^{i\omega_L t}$ is

$$\frac{\mathcal{I}_{\text{out}}}{\mathcal{E}_0^2} = \frac{2 + e^{i\phi_{\text{mod}}(t)} + e^{-i\phi_{\text{mod}}(t)}}{2} = \cos^2 \left(\frac{\phi_{\text{mod}}(t)}{2} \right) \quad (5)$$

and enables its use for intensity modulation at the operating point OP_1 for $V(t) \approx -\frac{V_\pi}{2}$ as suggested by Fig. 1(b). Assuming sinusoidal modulation $V(t) = -\frac{V_\pi}{2} + \frac{dV_\pi}{\pi} \cos(\Omega_{\text{mod}} t)$ around voltage $-V_\pi/2$ with modulation depth d we write the transfer function

$$\mathcal{T}(t) = \frac{\mathcal{E}_{\text{out}}(t)}{\mathcal{E}_{\text{in}}(t)} = \frac{e^{i\phi_0}}{2} (1 + e^{-\frac{i\pi}{2} + id \cos(\Omega_{\text{mod}} t)}). \quad (6)$$

The field transfer characteristic can be described in terms of the Bessel functions of the first kind \mathcal{J}_n using the Jacobi-Anger expansion

$$\frac{\mathcal{T}(t)}{e^{i\phi_0}} = \frac{1 - i\mathcal{J}_0(d)}{2} + \sum_{n=1}^{\infty} i^{n+1} \mathcal{J}_n(d) \cos(n\Omega_{\text{mod}} t), \quad (7)$$

which signifies that applying a low modulation depth d allows to cut off after the first time-dependent contribution. The Fourier components of Eq. (7) act as the driving terms \mathcal{T}_m in Eq. (4) of the main text. To ensure the validity of this cut-off, we compare the analytical intensity transfer function in Eq. (5) with the approximation resulting from truncating Eq. (7) after $n = 1$ in Fig. 1(c) in the parameter regime used in theory as well as the experiment. We note that one cannot indefinitely increase the modulation depth d to increase $|\tilde{\alpha}_{\pm 1}|^2$ and consequently the coupling related with $\sigma_{jl\pm 1}^{(0)} \sigma_{jl0}^{(\pm 1)}$ because the power will then be used to create sidebands $|\tilde{\alpha}_{\pm n}|^2$ at the frequencies $\omega_L \pm n\Omega_{\text{mod}}$ with $n > 1$.

III. RAMAN PICTURE DESCRIPTION

With the aim to provide further insight in the working principle of the stimulated emission processes, we first inspect the

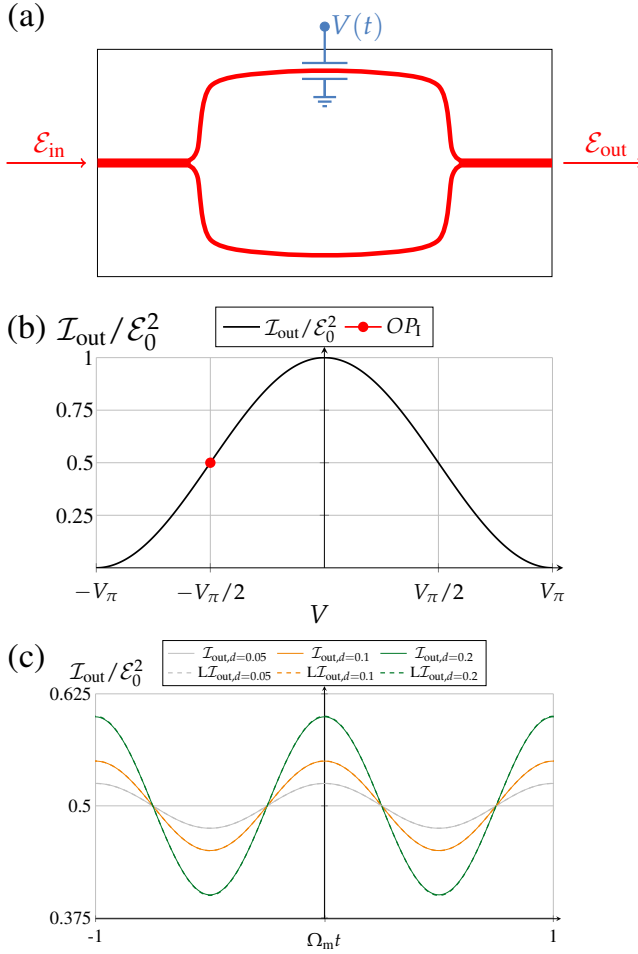


FIG. 1. Schematic description of a Mach–Zehnder intensity modulator. (a) Schematic diagram of a Mach–Zehnder interferometer and an electro-optic phase modulator implemented in one optical waveguides. (b) Resulting intensity transfer characteristic as a function of the applied voltage V on the electro-optic phase modulator. (c) Comparison of the intensity transfer function (solid) with the lowest order approximation (dashed) for periodic modulation with low modulation depth d .

effective decay rate including the process $\sigma_{jj0}^{(0)}(\Omega_j)$ but without periodic drive

$$\Gamma'_j = \Gamma_j + \frac{4\kappa g_j^2 |\bar{\alpha}_0|^2 \bar{\Delta} \Omega_j}{[\frac{\kappa^2}{4} + (\Omega_j - \bar{\Delta})^2][\frac{\kappa^2}{4} + (\Omega_j + \bar{\Delta})^2]}. \quad (8)$$

An example in the resolved sideband regime ($\kappa < \Omega_j$) is shown in Fig. 2(a) which illustrates that the initial phonon decay rate Γ_j can be counteracted by a phonon production process that is maximal for an effective detuning $\bar{\Delta} = \omega_{op} - \omega_L = -\Omega_j$. This means that the phonon production is most effective if drive photons entering the cavity carry the exact amount of excess energy $E = \hbar(\omega_L - \omega_{op})$ that is associated with one phonon $E_j = \hbar\Omega_j$, indicating that energy conservation of incoming and outgoing particles is the requirement for

the process. Therefore, we can visualize stimulated emission processes in an energy diagram with arrows pointing upwards as incoming particles and arrows pointing downwards as outgoing particles, as depicted in Fig. 2(b) and (c). The standard stimulated emission process displayed in Fig. 2(b) can be visualized by an incoming photon $(\bar{\alpha}_0)$ and a (stimulating) phonon \hat{b}_j which can be used to break down the photon into a resonant photon at the optical frequency and two phonons \hat{b}_j that inherit the phase from the stimulating phonon. Energy conservation of this process requires that the photon carries the excess energy of one phonon $\bar{\Delta} = -\Omega_j$.

The collaborative stimulated emission process $\sigma_{121}^{(0)}\sigma_{120}^{(1)}(\Omega_j)$ that is relevant for phase locked multi-mode oscillation in the numerical example is illustrated in Fig. 2(c). This process is associated with the decay rate alteration Eq. (6) in the main text. In the presence of modulation, the cavity is driven with carrier photons ($\bar{\alpha}_0$) at frequency ω_L that carrying excess energy $\bar{\Delta} = -\Omega_1$ as well as by photons in the modulation sidebands whose frequencies $\omega_L \pm \Omega_{mod}$ are either diminished ($\bar{\alpha}_{-1}$) or augmented ($\bar{\alpha}_1$) from the carrier frequency by the modulation frequency Ω_{mod} . A new process can be recognized that can be broken down into two subcycles:

1. The sideband photons ($\bar{\alpha}_1$) can be broken down by a stimulating phonon of mode 1 (\hat{b}_1) into a resonant photon and a new phase-locked phonon of mode 2 (\hat{b}_2). This process conserves energy if the photon's excess energy $-\hbar(\bar{\Delta} - \Omega_{mod})$ equals the energy $\hbar\Omega_2$ of a phonon in mode 2 which yields a condition for the modulation frequency $\Omega_{mod} = \Omega_2 + \bar{\Delta}$. Considering a central detuning $\bar{\Delta} = \omega_{op} - \omega_L = -\Omega_1$ this results in modulating at the difference of the mechanical frequencies $\Omega_{mod} = \Omega_2 - \Omega_1 \equiv \delta\Omega$.
2. This phase-locked phonon of mode 2 can in turn be used in a subsequent step to generate a new phonon of mode 1. This step requires a drive photon ($\bar{\alpha}_0$) with excess energy $-\hbar\bar{\Delta} = \hbar\Omega_1$ and the phase locked phonon in mode 2 (\hat{b}_2) to break down into a resonant photon and a phase locked phonon in mode 1 (\hat{b}_1) which can act as a stimulating phonon in the next cycle.

In total, we require one drive photon in the optical mode $\bar{\alpha}_0$, one drive photon in the optical mode $\bar{\alpha}_1$, and one stimulating phonon in \hat{b}_1 (e.g. thermal noise) to generate a new pair of phase locked phonons in the mechanical modes 1 and 2. This process can be attributed to the additional term $\sigma_{121}^{(0)}\sigma_{120}^{(1)}/[(\delta\Omega - \Omega_{mod}) + i(\Gamma_2/2) + \sigma_{121}^{(1)}]$ which appears in Eq. (6) of the main text. The collaborative stimulated emission requires that the driving occurs at the difference frequency and both stimulated emission processes are occurring with maximal rates for the effective detuning $\bar{\Delta} = -\Omega_1$ in this example. Therefore, adjusting the modulation frequency with optimal detuning only enables the collaborative stimulated emission process while the standard stimulated emission is already active. However, adjusting the detuning with an optimal modulation enables both stimulated emission processes simultaneously. We note that similar processes occur starting

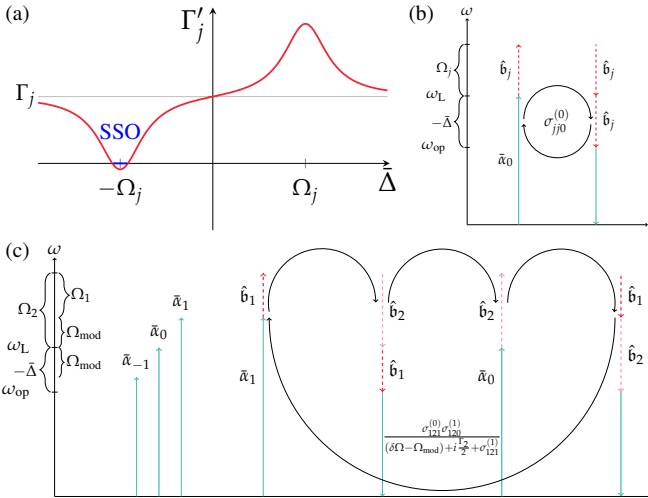


FIG. 2. Schematic diagrams of self-sustained oscillation (SSO) and multi-mode oscillation (MMO). (a) Effective phonon decay rate Γ'_j of a sideband resolved optomechanical system as a function of the effective detuning $\tilde{\Delta}$. The initial decay rate Γ_j is corrected by another process which can enhance or decrease the decay. If the drive photons' frequency ω_L exceed the optical cavity frequency ω_{op} by the frequency of a mechanical mode Ω_j the decay rate is minimal, indicating energy conservation as a requirement for stimulated emission (b) Schematic diagram based on energy conservation for self-sustained oscillation. In presence of a noise phonon of mode \hat{b}_j , a photon with the correct excess energy $\hbar\Omega_j$ can be broken down into a resonant photon and an additional phonon in the mode \hat{b}_j' sharing the phase of the original phonon. (c) Schematic diagram based on energy conservation for multi-mode oscillation. The intensity modulation generates photons with frequencies diminished ($\hat{\alpha}_{-1}$) or augmented ($\hat{\alpha}_1$) by the modulation frequency ω_{mod} from the central laser frequency ω_L taken to be $\omega_{\text{op}} + \Omega_1$. The initial step of the multi-mode lasing process breaks an augmented frequency photon ($\hat{\alpha}_1$) in presence of a noise phonon \hat{b}_1 down into a resonant photon and a phase locked phonon \hat{b}_2 in mode 2. This step is energy conserved if the modulation frequency is the difference of the mechanical frequencies $\delta\Omega = \Omega_2 - \Omega_1$. In the second step, this phase-locked phonon breaks up a photon ($\hat{\alpha}_0$) with the central frequency ω_L into a resonant photon and a phase locked phonon \hat{b}_1 in mode 1.

from a noise phonon in mode 2 at detuning $\tilde{\Delta} = -\Omega_2$ involving the other modulation sideband, all resulting in phase-locked generation of phonon pairs in the two modes.

IV. MUSICAL DESCRIPTION AND AURAL EVIDENCE OF MULTIMODE LASING

Another way of appreciating that a modulated drive can lead to phase locked oscillations at distinct frequencies can be drawn from music and more concretely from considering a conductor in charge of leading two groups. The natural frequencies of the mechanical modes in the numerical demonstration were chosen at a ratio $\Omega_2/\Omega_1 = 1.339 \approx 4/3$ such that coherent phase-locked oscillations can be identified with

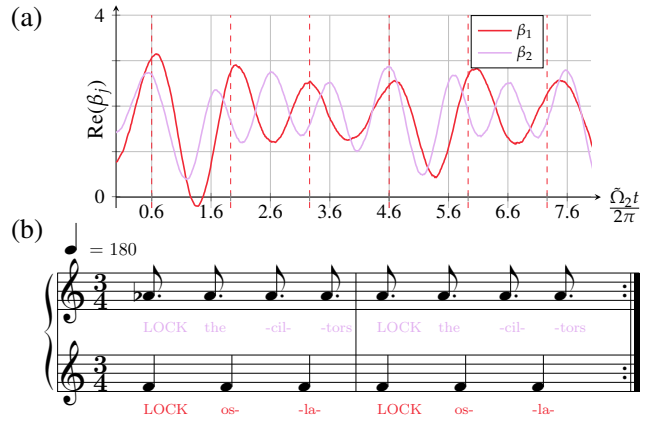


FIG. 3. A 4/3 polyrhythm as the musical analogon of multi mode lasing. (a) We show the mechanical traces in the MIMO state from Fig. 1(d) of the main text with the main vertical grid lines showing steps of $\tilde{\Omega}_2$ and therefore following the maxima of β_2 and the red dashed lines showing steps of $\tilde{\Omega}_1$ following the maxima of β_1 . Since the ratio of the frequencies is roughly 4/3 we expect that β_1 roughly completes 3 oscillations in the time that β_2 needs for 4 oscillations. (b) Musical notation of the 4/3 polyrhythm in which the lower voice plays three quarters in a three quarter measure such that the notes occur with a frequency of 3 Hz if there are 180 beats per minute. The higher voice plays four dotted eighth notes occurring with a frequency of 4 Hz which fit in the same measure. Additionally the lyrics indicate a mnemonic whose natural rhythm follows the rhythmical pattern. A potential conductor would indicate the beginning of each measure, coinciding with the syllable LOCK in both voices. This means that the conductor gives a sign to the two voices indicating the beginning of the measure occurring with a frequency 1 Hz which is the difference of 4 Hz and 3 Hz.

a so-called 4/3 polyrhythm as visualized in Fig. 3. A conductor usually indicates the beginning of a measure which is the smallest cyclic pattern of a musical piece. A measure is subdivided into pulses and here we assume a three quarter measure, i.e. a subdivision into three equal pulses. If a measure takes up one second, then each pulse takes up a third of a second. However, it is possible for a second voice to play four equidistant notes in the same time which are so-called dotted eighths and take up a quarter second each. This fits completely with our example since the two voices repeating notes at a frequency of 3 and 4 Hz are conducted by signs indicating a phase to lock to at the difference of these frequencies, namely at 1 Hz, like the conductor indicating the start of each measure. To validate the existence of multiple distinct frequencies in the oscillations of the mechanical modes, we use the displacement of the numerical simulations as seen in Fig. 1 of the main text to generate sound files. These result in a noisy tone for the thermal state, a single clear tone in the SSO state and in a two-tone chord in the MMO state. Since the natural frequencies are chosen approximately in a 4/3 ratio we expect to hear a so-called suspended fourth chord in the MMO state. We generated the sound files available as part of the supplemental material to certify oneself.

V. NUMERICAL ANALYSIS PROCEDURE AND PHASE DIAGRAM

We generate sample trajectories of our model such as those depicted in Fig. 1 of the main text by employing the Euler–Maruyama scheme [3] for the dynamics of the mean fields

$$\begin{aligned}\dot{\alpha} &= \left\{ -i \left[\Delta - \sum_{j=1}^N g_j R(\beta_j) \right] - \frac{\kappa}{2} \right\} \alpha + \mathcal{E}_0 \mathcal{T} e^{-i\phi_0} + \xi_\alpha(t), \\ \dot{\beta}_j &= - \left(i\Omega_j + \frac{\Gamma_j}{2} \right) \beta_j + ig_j |\alpha|^2 + \xi_{\beta_j}(t),\end{aligned}\quad (9)$$

where we choose the parameters of the two mechanical modes ($N = 2$) as described in the main text, namely $\Omega_1 = 5.3$, $\Gamma_1/\Omega_1 = 0.16$, $g_1 = 0.80$, $\Omega_2 = 7.1$, $\Gamma_2/\Omega_2 = 0.10$, $g_2 = 1.1$ as well as the optical cavity $\Delta = -6.1$, and $\kappa = 3$. This places the numerical example in the resolved sideband region such that only the collaborative stimulated emission process in Fig. 2(c) contributes and the similar process starting from a noise phonon in mode 2 mentioned above is suppressed. We keep all parameters within two orders of magnitude because stiff stochastic differential equations, having parameters varying over several orders of magnitude, cannot easily be simulated numerically. The Gaussian noise terms we employ are described by their statistical momenta, i.e. their mean $\langle \xi_s(t) \rangle = 0$ taken to be zero throughout the analysis and time correlation $\langle \xi_r(t) \xi_s(t') \rangle = \delta_{rs} \lambda_s \delta(t - t')$ for all $2(N+1)$ variables r and s denoting the real $\text{Re}(z) = R(z)/2$ and imaginary $\text{Im}(z) = I(z)/2$ parts of α and β_j with the variance of the Gaussian noise λ_s gauging the strength of the random forces. In order to generate realistic initial conditions of the system, we evolve the system starting from rest $\alpha(t = -t_0) = \beta_j(t = -t_0) = 0$ and without drive ($\mathcal{E}_0 = 0$) for an initial period of $t_0 = 100 \cdot \Omega_2 / (2\pi) \approx 115$ oscillation periods of Ω_2 emulating cavity shot noise, i.e. $\langle \xi_r(t) \xi_s(t') \rangle = (\delta_{\text{Re}(\alpha)r} + \delta_{\text{Im}(\alpha)r}) \delta_{rs} \delta(t - t')$. Note, that we neglect the equivalent quantum noise of the mechanical oscillator in the ground state because we aim to explore self-oscillating attractors of the nonlinear dynamics with the least energy possible in the system at initial time $t = 0$. After the initial procedure to thermalize the system, we then drive with $\mathcal{E}_0 = 8.9$, leading to $\bar{\Delta} \approx -\Omega_1$, and phonon noise $\langle \xi_r(t) \xi_s(t') \rangle = 0.01 \sum_j (\delta_{\text{Re}(\beta_j)r} + \delta_{\text{Im}(\beta_j)r}) \delta_{rs} \delta(t - t')$ to probe the stability of the attractor for $1000 \cdot \Omega_2 / (2\pi) \approx 1150$ oscillation periods of Ω_2 . The step size $\delta t = 0.0001$ throughout every simulation is chosen to be such that we have approximately 11500 sample points per oscillation period of Ω_2 in order to numerically converge. We conducted a larger parameter scan of the modulation depth d and the modulation frequency Ω_{mod} to understand the effects of the modulated drive. The numerical parameters are identical to the examples shown in Fig. 1 of the main text, apart from the modulation depth which is scanned from 0 to 0.1 in steps of 0.005, and the modulation frequency which is swept from 0 to 3 in steps of 0.05. The results are summarized in Fig. 4. The classification of a simulation into a thermal state (black square), self-sustained oscillation of one mode (blue square) or multi-

mode oscillation (red square) is based on the Fourier spectra of the mechanical displacements $\text{Re}(\beta_j)$ which were computed for $980 \cdot \Omega_2 / (2\pi) \approx 1100$ oscillation periods of Ω_2 . A simulation is classified as a thermal state if that all amplitudes in the range of ω between 4 and 10 are below the threshold value 10^{10} which can be seen in the inset of Fig 1.(b). Self-oscillation and multimode oscillation are related to a rise of the amplitude for either one or both mechanical displacements around their natural frequency above the threshold value 10^{11} . In addition, to classify a simulation as multimode oscillation, the maximal amplitude in the spectrum of the mechanical displacement of β_2 needs to be in the interval between 6 and 8 and a fit of the logarithm of a Lorentzian function $f(\omega) = \ln(\tilde{S}_0 + a[(\omega - \tilde{\Omega}_2)^2 + (\Gamma'_2/2)]^{-1})$ to the logarithm of the Fourier spectrum in that range results in a narrowed linewidth of $\Gamma'_2 < \Gamma_2/2$ while keeping the frequency $\tilde{\Omega}_2 = 6.8$ fixed. We see that increasing the modulation depth takes the system below laser threshold for low modulation frequencies. This can be understood since the total power that exits the Mach–Zehnder modulator is constant independent of the modulation depth and some of the power is taken from the main tone at ω_L to generate the two sidebands at $\omega_L \pm \Omega_{\text{mod}}$, which are not optimally detuned to generate lasing. If the modulation frequency is swept towards the difference frequency we see that the additional stimulated emission process first helps one mode to overcome the oscillation threshold and at the difference frequency and beyond the second mode also surpasses the threshold. The time requirements of the numerical algorithm limit the amount of simulations considered per data point leading to statistical fluctuations in the phase diagram. The white stars denote the modulation parameters for the shown simulations in Fig. 1 of the main text.

VI. QUALITATIVE DESCRIPTION OF HYSTERETIC BEHAVIOUR

The experimentally realized behavior of the multimode phonon lasing system shows hysteresis with the result that the MMO state can only be reached from the thermal steady state and not from one of the single-mode self-sustained oscillation states (SSO). The two experimental parameters which have to be controlled to achieve resonance in the correct order are the modulation frequency Ω_{mod} and the laser frequency which controls the detuning $\bar{\Delta}$. We find that the modulation frequency needs to be tuned to match the difference frequency first such that the collaborative processes $\sigma_{121}^{(0)} \sigma_{120}^{(1)}(\Omega_1)$ and $\sigma_{12-1}^{(0)} \sigma_{120}^{(-1)}(\Omega_2)$ are enabled before the detuning $\bar{\Delta}$ is tuned into resonance such that the four relevant stimulated emission processes $\sigma_{121}^{(0)} \sigma_{120}^{(1)}(\Omega_1)$, $\sigma_{12-1}^{(0)} \sigma_{120}^{(-1)}(\Omega_2)$, $\sigma_{110}^{(0)} \sigma_{110}^{(0)}(\Omega_1)$, and $\sigma_{220}^{(0)} \sigma_{220}^{(0)}(\Omega_2)$ are maximized altogether. If the detuning is tuned towards resonance without active intensity modulation the processes $\sigma_{110}^{(0)} \sigma_{110}^{(0)}(\Omega_1)$ and $\sigma_{220}^{(0)} \sigma_{220}^{(0)}(\Omega_2)$ lead to the mode competition mechanism which will end in the self-sustained oscillation of one mode only. Enabling the collaborative stimulated emis-

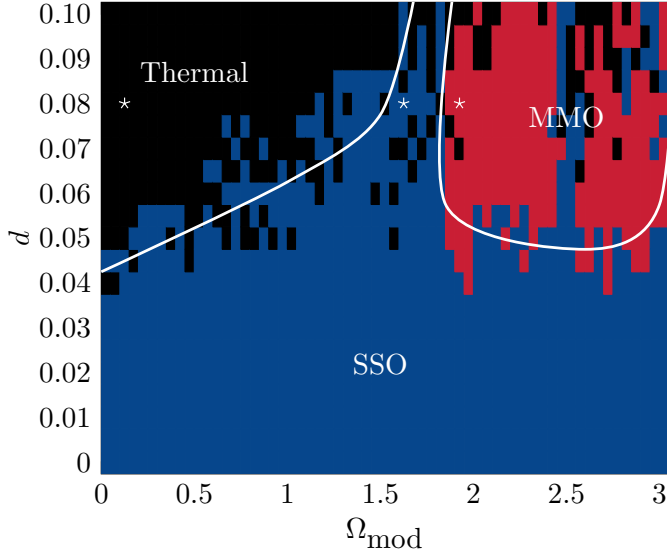


FIG. 4. Two-dimensional parameter scan of the modulation depth d and modulation frequency Ω_{mod} . For low modulation depths we find that the system goes into single mode self-sustained oscillation. Increasing the modulation depth for off-resonant modulation frequencies $\Omega_{\text{mod}} \ll \Omega_2 - \Omega_1$, the system is taken below the lasing threshold. For resonant modulation frequencies $\Omega_{\text{mod}} \approx \Omega_2 - \Omega_1$ we find multimode self-sustained oscillations. The fluctuations in the diagram are of statistical nature due to numerical constraints. The white stars denote the driving conditions taken for the simulations in Fig. 1 of the main text.

sion effects afterwards will not generate a flow into the MMO states basin of attraction which is strong enough to attract the system into the MMO state from the self-sustained oscillation attractors. The situation can be summarized in a commutative diagram as sketched in Fig. 5. The top left panel describes the situation for the initial parameters of the experiment. It allows for the thermal steady state as well as the distinct SSO states. Thermal fluctuations will randomize the initial condition around the thermal attractor such that instead of a singular point, we need to consider the probability distribution of initial states which is symbolized by the green and red disk around the thermal attractor. If neither the detuning nor the modulation frequency are resonant, the distributions are entirely enclosed in the thermal state's basin of attraction. If we follow the commutative diagram in the counter-clock wise direction, we follow the evolution of the green disc. It follows the dynamical flow under the change of the modulation frequency first. Since we enable the higher order ($\propto g_j^2 g_l^2$) processes $\sigma_{121}^{(0)} \sigma_{120}^{(1)}(\Omega_1)$ and $\sigma_{12-1}^{(0)} \sigma_{120}^{(-1)}(\Omega_2)$, the basin of attraction of the thermal state will only shrink weakly compared to the other processes ($\propto g_j^2$) but it will generate the additional MMO attractor. Resonantly modifying the detuning will destabilize the thermal attractor and the green disk will flow partly to the MMO state. If we exchange the order and follow the commutative diagram in the clock-wise direction we follow the evolution of the red disc. Here, the de-

tuning is turned into resonance such that the thermal attractor is destabilized immediately. However, the higher order processes are off-resonant and therefore suppressed such that the standard mode-competition setting holds. The red disc flows partly into each SSO attractor. Tuning the modulation frequency into resonance now will create the MMO attractor but its basin of attraction is too far away for thermal fluctuations around the SSO states to enable flow into the MMO state.

VII. THE ROLE OF THE OPTICAL SPRING EFFECT IN FREQUENCY STABILITY

One effect that could play a role in the observed frequency stabilization in the MMO state is related to fluctuations transduced through the optical spring effect. To understand this in more detail, consider the central frequency corrected by the optical spring shift to Ω'_j due to the process $\sigma_{jj0}^{(0)}(\Omega_j)$ which is found to be

$$\Omega'_j(\Omega_j) = \Omega_j \sqrt{1 - \frac{\bar{\Delta}g_j^2 |\bar{a}_0|^2 [\frac{\kappa^2}{4} - \Omega_j^2 + \bar{\Delta}^2]}{\Omega_j [\frac{\kappa^2}{4} + (\Omega_j - \bar{\Delta})^2] [\frac{\kappa^2}{4} + (\Omega_j + \bar{\Delta})^2]}}. \quad (10)$$

Observing that $|\Omega'_j - \Omega_j| \ll \Omega_j$, we apply the Taylor expansion $\sqrt{1 - ax^2} \approx 1 - \frac{ax^2}{2}$ leading to the approximated central frequency

$$\Omega'_j(\Omega_j) \approx \Omega_j - \frac{\bar{\Delta}g_j^2 |\bar{a}_0|^2 [\frac{\kappa^2}{4} - \Omega_j^2 + \bar{\Delta}^2]}{2[\frac{\kappa^2}{4} + (\Omega_j - \bar{\Delta})^2][\frac{\kappa^2}{4} + (\Omega_j + \bar{\Delta})^2]}. \quad (11)$$

A change of laser intensity $|\bar{a}_0|^2$ by an amount δI leads to a change of the mechanical frequency

$$\delta\Omega'_j = -\frac{\bar{\Delta}g_j^2 [\frac{\kappa^2}{4} - \Omega_j^2 + \bar{\Delta}^2]}{2[\frac{\kappa^2}{4} + (\Omega_j - \bar{\Delta})^2][\frac{\kappa^2}{4} + (\Omega_j + \bar{\Delta})^2]} \delta I. \quad (12)$$

As such, laser intensity fluctuations, either quantum fluctuations or classical fluctuations related to the laser or the tapered optical fiber, could affect the stability of the mechanical resonator through the induced optical spring shift. Moreover, uncertainty in other quantities such as the detuning $\bar{\Delta}$ contributes with additional error. The thermo-optic effect, which leads to laser-induced cavity red-shift in the silicon nanocavities we employ, stabilizes fluctuations in intensity and detuning only to a finite degree. The magnitude of the resulting spring shift depends on the mean intracavity photon number. A reduction of the intracavity photon number as suggested by the theoretical finding that the lasing threshold power is lowered by the modulation as seen in the phase diagram, and the observed reduction of the peaks in the experimental spectra in the MMO state, are consistent with the hypothesis that this mechanism contributes to the observed stabilization.

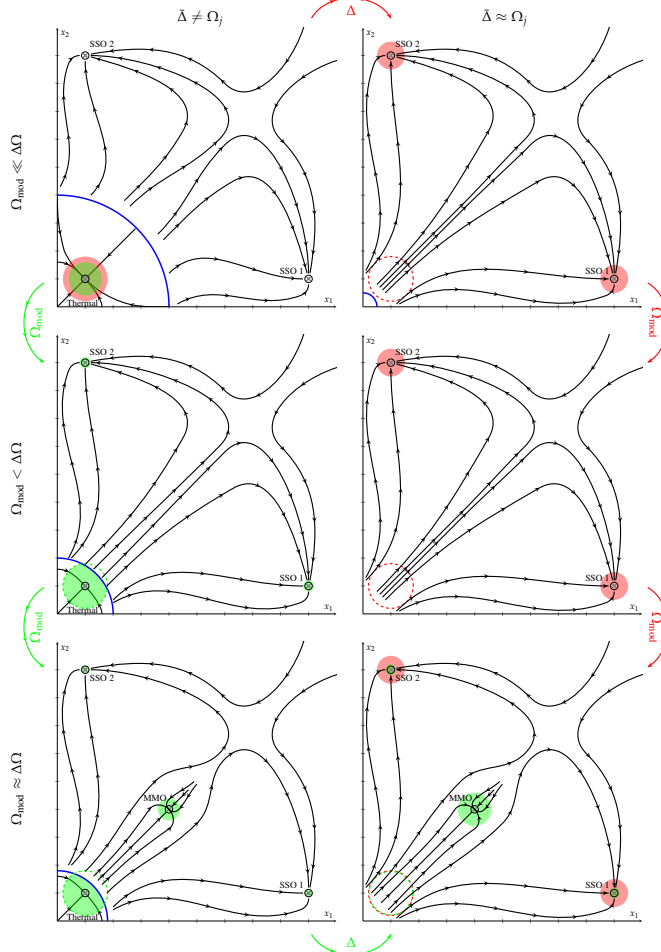


FIG. 5. Commutative diagram sketch encompassing the experimentally realized lasing behaviour. The initial parameters in the top left panel allow for a thermal steady state (“Thermal”), delineated by the blue line, and self-sustained oscillation of each mechanical mode (“SSO1” and “SSO2”). Thermal fluctuations lead to the distribution of the initial condition described by the green and red disk. Going counter-clockwise to the final state in the bottom right corner shows how to create the MMO state. First adjusting the modulation frequency creates the MMO attractor in the middle of the panel without destroying the thermal attractor. Turning the detuning into resonance then sets the initial probability distribution into motion following the flow with the possibility to be drawn into the MMO’s basin of attraction. Going clockwise to the final state, i.e., following the red path, shows that tuning the detuning toward resonance immediately destroys the thermal state forcing the oscillators into either SSO attractor as in the mode competition setting. Creating the MMO attractor afterwards cannot pull the probability distributions of the final state into its basin of attraction.

VIII. EXPERIMENTAL SETUP

The measurements were performed with the experimental setup illustrated in Fig. 6. Two similar setups were installed (independently) at the AMOLF institute in the Netherlands and the Nanophotonics Technology Center (NTC) in Spain,

where different compatible and reproducible sets of measurements were obtained. All the measurements presented in this work were taken on the same optomechanical crystal cavity sample. A tunable fiber-coupled external cavity diode laser (New Focus TLB-6728) generates a continuous-wave optical signal that passes through an intensity modulator fed by a signal generator (SG) with a tuneable modulation frequency ω_{RF} . In both setups the used intensity modulator was a Covagema Mach MZM and the SG was an EXG Analog Signal Generator N5173B at AMOLF and an Agilent E4438C ESG Vector Signal Generator at NTC. The modulated laser signal is passed through an erbium doped fiber amplifier (EDFA), a polarization controller (PC), and an optical circulator before it is sent into a dimpled tapered fiber. Another employed version of the system consists in coupling the light into and out of the cavity with a fiber taper loop. When the dimpled fiber is close enough to the OM cavity under study, light is coupled evanescently from the fiber to the cavity so that we can characterize both the transmission and reflection spectra, shaded/highlighted in red and blue, respectively.

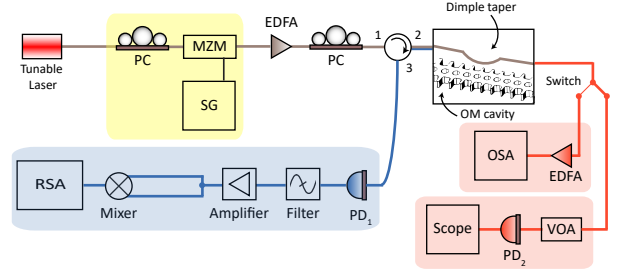


FIG. 6. Schematic of the experimental setup used in the multimode experiment lasing.

The transmitted signal is first sent to a variable optical attenuator (VOA), where it is photodetected (PD_1) to monitor the optical resonance with an oscilloscope (‘Scope’). The reflected signal is photodetected after the circulator via a 12 GHz Photodetector (New Focus 1544-B DC-Coupled NIR Fiber-Optic Receiver) (PD_2) and then filtered with a band pass filter (Mini-Circuits VBFZ-4000-S+). This filter is used to suppress the modulated frequency ω_{RF} in the detected electrical signal which would overlap with the difference tone. Once the low frequency range has been filtered, the signal is electrically amplified (Miteq MPN4-02001800-23P) and divided (Mini-Circuits 15542 ZFRSC-42) in order to feed the two input ports of an electrical mixer (MACOM M63C), where the difference and sum tones of the two lasing mechanical modes P1 and P2 are created. Finally, the resulting signal is analyzed with a radiofrequency spectrum analyzer (RSA). The RSA used at AMOLF was a MXA Signal Analyzer N9020A and at NTC a Anritsu MS2850A Signal Analyzer. All the phase noise measurements presented in this work were obtained with the latter one. Real-time spectrograms of the spectrum versus time were acquired on both.

To reach the MMO regime the experiment was performed

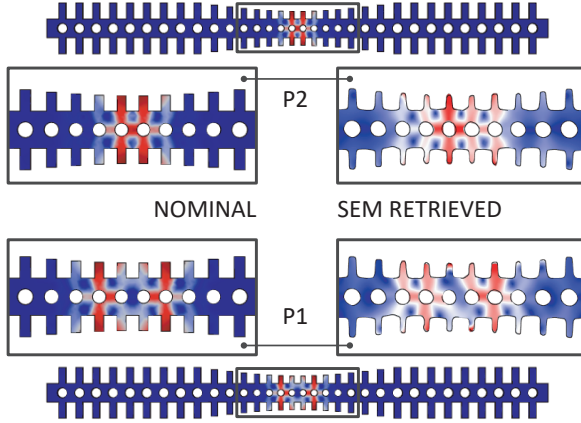


FIG. 7. Comparison of the mechanical mode profile of the nominal structures and the final fabricated profile structure for the two mechanical modes involved in the experiments.

as follows: First, the difference frequency between the two involved mechanical modes was characterized at different laser wavelengths. Next, this difference frequency was set as the modulation frequency of the laser driving the cavity, and it was kept constant in the rest of the experiment. Finally, a sweep of the laser wavelength on the blue-detuned side of the resonance was performed, reaching in this way the self-oscillation regime in the MMO state.

The difference tone $\Omega_2 - \Omega_1$ is also measured with this experimental setup to confirm the mode-locking between P1 and P2. This is achieved by sending the detected signal through the microwave mixer. Using a control measurement, we verified that the filter fully suppresses the (low-frequency) optical modulation frequency recorded by the photodetector, such that the measured difference-frequency signal was only related to the mixing of the two GHz-frequency signals of the oscillators P1 and P2.

IX. MECHANICAL MODE CHARACTERIZATION

Because of fabrication imperfections, the final structures differ from the nominal ones. In order to ensure that the measured mechanical modes were still located in the middle region of the cavity, a calculation of the mechanical modes was performed using a profile retrieved from a Scanning Microscopy Image (SEM). In Fig. 7 both the theoretical mechanical mode profile of the nominal structure and the real profile fabricated structure are compared. Here, we can see similarity between the two profiles of the mechanical modes in both cases. Regarding the mechanical properties of the system, from the thermally-transduced mechanical mode measurements, the linewidths of the involved mechanical modes are $\Gamma_1/2\pi = (2.7 \pm 0.2)$ MHz and $\Gamma_2/2\pi = (2.26 \pm 0.12)$ MHz and the optomechanical coupling rates $g_1/2\pi = (606 \pm 14)$ kHz and $g_2/2\pi = (687 \pm 16)$ kHz.

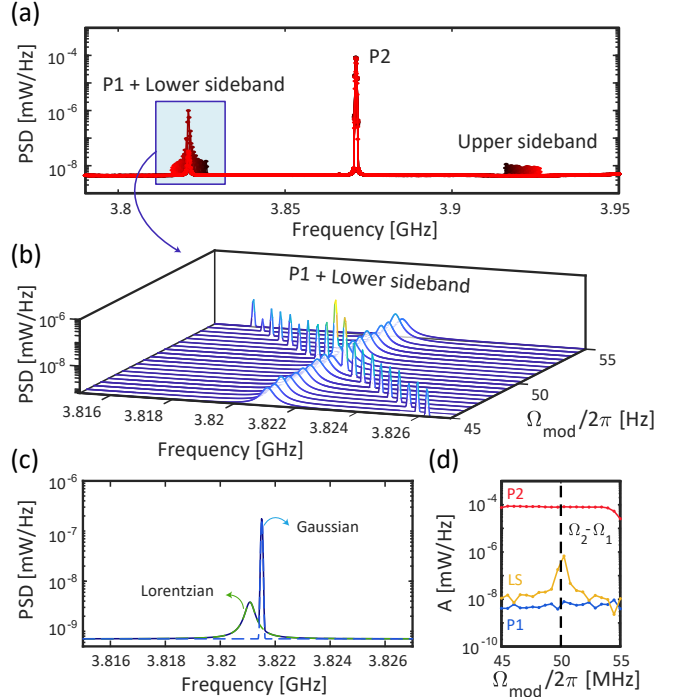


FIG. 8. Modulation frequency scan. (a) Overview of the upconversion of the modulation tone around $\Omega_2 - \Omega_1$. (b) Close view of the scan of the modulation tone around P1. (c) Example of the different fit contributions in the overlap between P2 and the lower sideband. (d) Evolution of the amplitudes of P1, P2 and the lower sideband as a function of the modulation frequency tone.

X. MODULATION FREQUENCY SCAN

Once P1 or P2 is in the lasing state, an upconversion of the drive modulation tone occurs. This means that the drive tone gives rise to a lower and an upper sideband of the lasing tone in the optical modulation spectrum. This can be seen in Fig. 8(a), which shows many spectra (colored from black to red) that are taken while varying the modulation frequency around the difference frequency of P1 and P2. A close view of this scan is shown in Fig. 8(b). Here, we can see that for modulation frequencies around $\Omega_2 - \Omega_1$, the lower sideband (LS) overlaps with the mechanical mode P1. In order to observe whether the mechanical modes P2 or P1 experience a change, we analyzed the amplitude of those modes and the lower sideband. It has to be noted that in the case of the overlap between P1 and the lower sideband, we have performed a fit of a Lorentzian in the case of the thermally driven mechanical mode P1 and a fit of a Gaussian in the case of the lower sideband driven by modulation tone as can be seen in Fig. 8(c). We find that the linewidth of the Lorentzian (P1) is never narrowed while the modulation sideband of P2 is scanned in and out of resonance with mode P1. This shows that the MMO state cannot be reached from the SSO state. The resulting evolution of both P1, P2 and LS amplitudes are presented in Fig. 8(d).

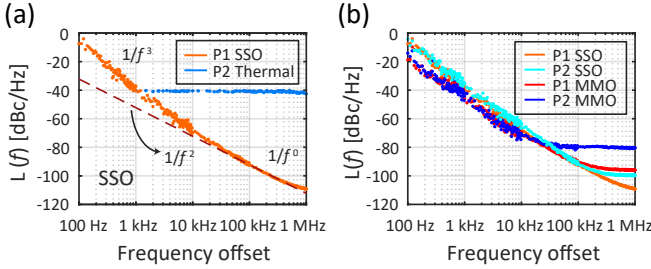


FIG. 9. (a) Phase noise $L(f)$ from a thermally driven mechanical mode and a SSO mode. (b) Comparison of the two mechanical modes P1 and P2 in the SSO and MMO states.

XI. PHASE NOISE MEASUREMENTS

The phase noise measurements from 100 Hz to 1 MHz frequency offset were performed with an Anritsu MS2850A Signal Analyzer, as mentioned above. A measurement of the phase noise of a mechanical mode thermally driven and a SSO mode was performed in order to be able to distinguish both situations. These measurements are presented in Fig. 9(a) for the case where P1 is self-oscillating. Here, we can see an appreciable difference between these two cases as the thermally driven mode had a very low amplitude, thus resulting in a huge contribution of frequency noise sources related to the white phase noise.

On the other hand, Fig. 9(b) shows a comparison of the phase noise for all the cases of the mechanical modes P1 and P2. P1 SSO and P2 SSO were taken when the corresponding mechanical modes were in the self-oscillation state and P1 MMO and P2 MMO were taken when both of them were simultaneously oscillating. As discussed in the main text, the most interesting feature arises in the low frequency offset regime, where we can see a difference in the phase noise from SSO and MMO. For all frequencies below ~ 10 kHz (where the white noise background is insignificant), the phase noise improves when the two mechanical modes are in the multi-mode regime. For these frequencies, the phase noise has a largest contribution related to flicker frequency noise, judging from the slope of this curve.

XII. ALLAN DEVIATION CALCULATION

The calculation of the Allan deviation $\sigma_y(\tau)$ was performed in two different ways. For small averaging times τ , the parameter was derived from the phase noise data as [4]:

$$\sigma_y(\tau) = \sqrt{\int_0^\infty \frac{4f^2 L(f)}{f_c^2} \frac{\sin^4(\pi\tau f)}{(\pi\tau f)^2} df}, \quad (13)$$

where $L(f)$ is the measured phase noise and f_c the carrier frequency of the oscillator under study.

Figure 10(a) shows the common SSB phase noise $L(f)$. However, the most common quantity to describe the oscil-

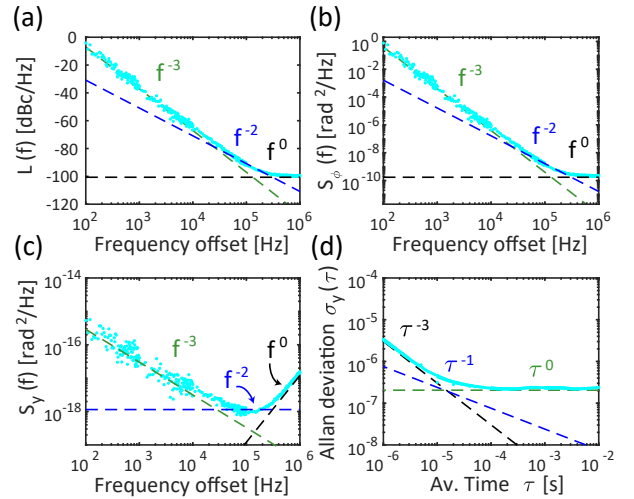


FIG. 10. P2 SSO Noise type contributions. (a) Phase noise $L(f)$. (b) Phase noise $S_\varphi(f)$. (c) Frequency noise $S_y(f)$. (d) Allan deviation $\sigma(\tau)$. The phase noise fit contributions described by Leeson's model for the frequency and time domain are indicated with dashed lines.

lator phase noise is $S_\varphi(f)$ which can easily be derived as $S_\varphi(f) = 2L(f)$. In order to derive $\sigma(\tau)$ an auxiliary parameter $S_y(f)$ is also needed, which is related to the physical parameter $S_\varphi(f)$ as

$$S_y(f) = \frac{f^2}{f_c^2} S_\varphi(f). \quad (14)$$

The phase noise shows the typical dependencies, with $1/f^3$ (flicker frequency noise, lower part of the spectrum Fig. 10(a,b)), $1/f^2$ (white frequency noise, upper part of the spectrum in Fig. 10(a,b)) and white noise $1/f^0$, which are in good agreement with the general phase noise described by the Leeson's model [5, 7].

Besides the phase noise as a measure about the stability of a signal, we can also study the root mean square (RMS) jitter (J_{RMS}). It can be obtained by integrating the phase noise power data as [4]:

$$J_{RMS} = \frac{1}{2\pi\nu_0} \sqrt{2 \int_{f_1}^{f_2} 10^{\mathcal{L}(f)/10} df} \quad (15)$$

where f_1 and f_2 are the start and stop frequency, respectively.

On the other hand, for the long-term stability another approach was followed, in order to characterize the frequency drift of our oscillators. Besides the approximation of the calculation of the Allan deviation from the phase noise, this stability measurement can also be described as [6]

$$\sigma_y(\tau) = \sqrt{\frac{1}{2M} \sum_{i=0}^{M-1} (y_{i+1} - y_i)^2} \quad (16)$$

where $M = T/\tau - 1$ and $y_i = (\langle f_1(t_0 + i\tau) \rangle_\tau - f_c)/f_c$. Here, $\langle f_1 \rangle_\tau$ is the average frequency of the system over the interval τ .

In our experiment, the measurement of the evolution of the

frequency as a function of time was performed with a real time electrical spectrum analyzer over a total measurement time of 1 s and a timing step around 1 ms.

-
- [1] B. E. A. Saleh and M. C. Teich *Fundamentals of Photonics* (Wiley, 1991).
 - [2] M. Seimetz *High-Order Modulation for Optical Fiber Transmission* (Springer, 2009).
 - [3] P. E. Kloeden and E. Platen, *Numerical Solution of Stochastic Differential Equations* (Springer-Verlag, Berlin-Heidelberg, 1992).
 - [4] X. Luan, Y. Huang, Y. Li, J. F. McMillan, J. Zheng, S. Huang, P. Hsieh, T. Gu, D. Wang, A. Hati, D. A. Howe, G. Wen, M. Yu, G. Lo, D. Kwong, and C. W. Wong, *Sci. Rep.* **4**, 6842 (2014).
 - [5] E Rubiola *Phase Noise and frequency stability in oscillators* (Cambridge University Press, 2009).
 - [6] W. Yu, W. C. Jiang, Q. Lin and T. Lu, *Nat. Commun.* **7**, 12311 (2016).
 - [7] L. Mercadé, L. L. Martín, A. Griol, D. Navarro-Urrios and A. Martínez, *Nanophotonics* **9**, 11 (2020).